

Cite this: *Phys. Chem. Chem. Phys.*, 2013, **15**, 10385

Electronic structures and magnetic properties of MoS₂ nanostructures: atomic defects, nanoholes, nanodots and antidots

Yungang Zhou,^{*a} Ping Yang,^b Haoyue Zu,^a Fei Gao^{*b} and Xiaotao Zu^{*a}

Developing approaches to effectively induce and control the magnetic states is critical to the use of magnetic nanostructures in quantum information devices but is still challenging. Here MoS₂-based nanostructures including atomic defects, nanoholes, nanodots and antidots are characterized with spin-polarized density functional theory. The S-vacancy defect is more likely to form than the Mo-vacancy defect due to the form of Mo–Mo metallic bonds. Among different shaped nanoholes and nanodots, triangle ones associated with ferromagnetic characteristic are most energetically favorable, and exhibit unexpected large spin moments that scale linearly with edged length. In particular, S-terminated triangle nanodots show strong spin anisotropy around the Fermi level with a substantial collective characteristic of spin states at edges, enabling it to a desired spin-filtering structure. However, in the antidot, the net spin, coupled order and stability of spin states can be engineered by controlling type and distance of internal nanoholes. Based on the analysis of the spin coupled mechanism, a specific antidot structure, the only S-terminated antidot, was determined to exhibit a large net spin with long-range ferromagnetic coupling above room temperature. Given the recent achievement of graphene- and BN-based nanohole, nanodot and antidot structures, we believe that our calculated results are suitable for experimental verification and implementation opening a new path to explore MoS₂-based magnetic nanostructures.

Received 27th January 2013,
Accepted 18th April 2013

DOI: 10.1039/c3cp50381j

www.rsc.org/pccp

1. Introduction

In the wake of extensive research on graphene, the two-dimensional (2D) transition-metal dichalcogenides (TMDs) of TX₂ type (T = Mo, W, Nb, Re, Ti, Ta, *etc.*, X = S, Se, Te) with a thickness down to three atomic layers have become particularly interesting because of the large variety of electronic phases that they can exhibit, namely, metallic,^{1–3} semiconductor,^{4–7} and superconductor.⁸ Following the successful fabrication by hydrothermal processes⁹ and mechanical activation at high temperature,¹⁰ TMDs attract considerable experimental attention as proposals for novel electronic devices. The possible applications of these materials, such as transistors,^{11,12} photoemitting devices,¹³ photovoltaics,¹⁴ catalysis,¹⁵ hydrogen storage,¹⁶ lubricants,¹⁷ and Li-ion batteries^{18,19} have been proposed and investigated. Several recent theoretical

articles have explored various aspects of 2D nanostructures, for example, electron phonon coupling,^{20,21} detection of edge states,^{22–29} band structure engineering,^{30–32} and interaction with substrates.^{33,34} Developing approaches to effectively induce and manipulate the magnetic states are critical to the use of magnetic nanostructures in quantum information devices. However, the systematic exploration of novel magnetic characteristics in TMD-based structures so far is still limited. As a matter of fact, most pristine TMDs are nonmagnetic. Previous studies to induce and engineer the magnetism into the nonmagnetic TMDs nanostructures mainly focused on chemical functionalization,³⁵ applying an external strain to the 2D TMD sheets,³⁶ or giving an external static electric field on TMD nanoribbons.³⁷

Here, another approach, *i.e.*, by fabricating the TMD morphology, to induce spontaneous magnetism in 2D TMD materials was employed, which allows us to go beyond the current scope limited to the spins within graphene- and BN-based 2D nanostructures. In general, there are two ways where spontaneous magnetism can arise by fabricating the TMD morphology. First local magnetism can arise if the isolated atomic defects exist. For example, the C-vacancy (C_v)

^a Department of Applied Physics, University of Electronic Science and Technology of China, Chengdu, 610054, P.R. China. E-mail: zhouyungang1@126.com, xtz@uestc.edu.cn

^b Pacific Northwest National Laboratory, MS K8-93, P.O. Box 999, Richland, Washington 99352, USA. E-mail: fei.gao@pnl.gov

in graphene can be magnetized, with a magnetic moment that increases from 1.12 to 1.53 μ_B as the defect concentration decreases from 20% to 0.5%.³⁸ In the BN sheet, a single B-vacancy (V_B) can induce a spin polarization of 0.29 μ_B in the neighbor N atom, while a single N-vacancy (V_N) has very small influence on the magnetic property.³⁹ Second, if TMDs can be fabricated to exhibit a high density of edge terminations, spontaneous magnetism may arise at the edges due to the different Mo and S coordinations. For example, zigzag MoS_2 nanoribbons have been detected to exhibit the ferromagnetic (FM) and metallic characteristics, irrespective of the ribbon width and thickness.⁴⁰ In similar literatures, such as BN, AlN and graphene nanoribbons, zigzag edged N atoms in BN and AlN ribbons were found to display a giant spin splitting with a 100% spin polarization near the Fermi level, while the net spins of zigzag edged B atoms in the BN ribbon, Al atoms in the AlN ribbon, and C atoms in the graphene ribbon were zero due to the antiferromagnetic (AFM) coupling.^{41–43} In particular, all zigzag edges in triangular graphene and BN nanodots can be metallic ferromagnetic, in which the net spin can increase linearly with the size.^{44,45} Recent theoretical studies on graphene and BN nanoholes also predicted the remarkable magnetic moment, mainly contributed by zigzag edged unpaired atoms, and the magnitude of the magnetism can be tuned by varying the parameters of hole shape, the hole size, and the hole separation.^{45,46} Thus, these studies suggest that fabricating structural morphology can be potentially used as an effective pathway to induce and manipulate the magnetic properties, which stimulates us to systematically understand the magnetic behaviors in TMD-based nanostructures.

Although the experimental direct evidence to detect the defects with zigzag edge in TMDs-based nanostructure so far is little, the defect structures in 2D nanomaterials have also been subject to recent research.^{47,48} Furthermore, an experimental study of TMD-based nanostructures can be facilitated by recent advances in nanolithographic techniques, such as electron beam or focused-ion-beam writing^{49,50} and X-ray or extreme-UV lithography,⁵¹ where the desired defect structure can be achieved on nanostructures in a controlled way. For example, atomic defects,^{52–54} nanoholes,^{55,56} nanodots,⁵⁷ and antidots⁵⁸ in graphene- and BN-based nanostructures have been successfully fabricated and detected in the research laboratory. Thus, we believe that our calculated results are suitable for experimental verification and implementation opening a new path to explore the magnetic devices in TMD-based nanostructures.

The present study is prompted by the recent observation of atomic defects in MoS_2 sheet⁵⁹ and triangle MoS_2 nanodots with zigzag edges,⁶⁰ and as such may be anticipated to carry large magnetic moments as reported in literatures of BN, AlN and GaN-based nanostructures.^{39,41,43} Based on spin-polarized *ab initio* density functional theory, we systematically explore structural stability, electronic and magnetic properties of MoS_2 -based nanostructures, such as atomic defects, nanoholes, nanodots and antidots, as an example of TMD systems. This paper is organized as follows: (i) we presented a brief discussion of the

properties of a perfect MoS_2 sheet whose structural parameters were compared with previous studies. (ii) We examined the stability of atomic defects, and found that the S-vacancy defect was most energetically favorable in all S conditions, which may clarify the preferred origin for the further formation of nanoholes. (iii) We investigated the stability of different shaped nanoholes. Especially, we determined the magnetic properties of these structures due to the unpaired edged atoms. The effect of the reconstruction of corner atoms on the stability and magnetic properties of MoS_2 nanoholes was evaluated. (iv) We calculated the stability and magnetic properties of different shaped nanodots, and proposed a possible application of nanodots in excellent spin transmission channel. (v) We analyzed the spin coupling characteristics of antidots, and deduced a possibility to achieve the larger magnetism above room temperature. Thus our study reveals interesting results, which are important for further study and applications of MoS_2 -based magnetic nanodevices.

2. Computational methods

The first principle periodic calculations based on density functional theory (DFT) were performed using the Vienna *ab initio* simulation package (VASP). Within the generalized gradient approximation (GGA), we considered the Perdew-Burke-Ernzerhof (PBE) exchange and correlation functionals. The electronic wave functions were expanded using a plane-wave basis set with a cutoff energy of 550 eV. In our calculations, the different shaped nanodots with zigzag edges were established in a supercell of $32 \times 32 \times 15 \text{ \AA}$, which is sufficiently large to avoid the interactions between the adjacent nanodots. The brillouin zone integration with a $1 \times 1 \times 1$ k -point grid was used to optimize these structures. For the total energy calculation of nanoholes, we considered an $8 \times 8 \times 1$ supercell related with $4 \times 4 \times 1$ k -point grid. However, for the simulation of antidots, a $12 \times 12 \times 1$ supercell related with $2 \times 2 \times 1$ k -point grid was used. A large spacing of 15 \AA between the MoS_2 planes is taken to prevent interactions. All atomic positions and lattice constants are optimized by using the conjugate gradient method, where the total energy and atomic forces are minimized. The calculations were carried out with spin-polarization, and the atomic positions of the structure were relaxed until all the force components were smaller than 0.01 eV \AA^{-1} .

3. Results and discussion

3.1 Perfect MoS_2 sheet

For the sake of comparison with previous studies, we first present a brief discussion of the properties of the perfect MoS_2 sheet. Each MoS_2 sheet is trilayered with a Mo atom in the middle that is covalently bonded to six S atoms located in the top and bottom layers. The optimized structural parameters, such as lattice constant $a = 3.16 \text{ \AA}$, bond distance between S and Mo atoms $d_{\text{S-Mo}} = 2.41 \text{ \AA}$, the distance between top and bottom S layers $d_{\text{S-S}} = 3.13 \text{ \AA}$, and the S-Mo-S angle $\theta_{\text{S-Mo-S}} = 80.7^\circ$, are well in agreement with recent theoretical reports.^{35,61,62}

Similar to the BN sheet, the MoS₂ sheet also contains an ion characteristic due to the electronegativity difference between S and Mo atoms, and thus the strong directional effect of bonding confinement dominates the property of a direct bandgap (1.7 eV). Perfect MoS₂ sheet is a nonmagnetic nanomaterial, and the finding of the ideal bandgap gives a potential for its applications in electronics. The valence-band maximum (VBM) and the conduction-band minimum (CBM) are dominated by the hybridization of Mo-4d and S-3p orbitals.

3.2 Atomic defects in MoS₂ sheet

Previous theoretical results of graphene and BN sheet revealed that atomic defects in low-dimensional materials are quite important since they strongly affect material magnetic properties.^{38,39} Thus, we first characterized the properties of atomic defects in the MoS₂ sheet. Here the S-vacancy (V_S) and Mo-vacancy (V_{Mo}) were created by removing double S and single Mo atoms, respectively, from a MoS₂ supercell. The geometries were subsequently optimized and the formation energies were calculated. Our calculations show that both vacancies can induce a structural deformation along the MoS₂ flat plane but without any bulking in perpendicular direction, as shown in Fig. 1(a), which plays an important role in the structural stability and magnetic magnitude. In order to determine the relative stability of defect structures, the formation energy was calculated, as shown in Fig. 1(b). Here the formation energy (E_f) of the vacancy at the site i ($i = S, Mo$) in MoS₂ sheet is given by the expression:

$$E_f = \left(E_V + \sum n_i \mu_i - E_{MoS_2} \right) \quad (1)$$

where E_V and E_{MoS_2} are total energies of the supercell with and without vacancy defect, μ_i ($i = S, Mo$) and n_i are the chemical potential and number of the removed i atom. It is well known that the choice of μ_i is normally defined by the growth conditions of a material. In Fig. 1(b), arrows at the left and right boundaries of μ_S correspond to two typical experimental

conditions that use bulk Mo and Brenstone as the reservoirs, respectively. In the S-rich environment, we calculated the E_f of V_S is 2.9 eV, about 1.1 eV lower than that of the V_{Mo} defect. In the S-poor environment (equivalently, Mo-rich conditions), the E_f of V_S becomes 1.3 eV, about 6.0 eV lower than that of the V_{Mo} defect. Thus, the V_S defect is more likely to form than the V_{Mo} one in both environments, and might as the main native defect for the further formation of nanoholes. As a matter of fact, the difference of stability between the two structures can be qualitatively characterized by the geometry changes, as shown in Fig. 1(a). For example, in the V_{Mo} structure, three S atoms closest to the vacancy move apart from each other forming a large triangle like structure after optimization. V_{Mo} -neighbor S-S distances (d_{S-S}) become 3.34 Å, which is 0.18 Å larger than that of the perfect MoS₂ sheet. Obviously, V_{Mo} leaves three unfavorable S radicals behind, and these S radicals are hard to bound, enhancing the energy. In contrast, in V_S structure, three Mo atoms closed to the vacancy move closer to each other forming a small triangle like structure. V_S -neighbor Mo-Mo bond lengths (d_{Mo-Mo}) become 2.80 Å, 0.36 Å shorter than that of the perfect MoS₂ sheet and compared with that of Mo bulk (2.7 Å). Thus, the removal of the S atom leads to unfavorable Mo radicals to form the additional metal bond because of the small Mo-Mo distance, lowering the energy significantly. The finding of structural deformation induced by vacancy is similar to that in the BN sheet where the V_N -neighbor B-B bond lengths (d_{B-B}) become about 2.10 Å (0.40 Å smaller than that of the perfect BN sheet) and V_B -neighbor N-N bond lengths (d_{N-N}) become about 2.70 Å (0.20 Å greater than that of perfect BN sheet⁶³). In fact, the lowering of energy due to removal of radicals has been previously reported to explain the high stability of the large vacancy clusters in graphene.⁶⁴

As reported in graphene and BN sheets,^{38,39} with the removal of one atom in the sheet structure, each of the three vacancy-neighbor atoms can possess the unpaired electrons, which could produce the magnetism. Possible applications of magnetic behaviors induced by vacancy defect have been extensively reported. However, the situation in the MoS₂ structure is somewhat different. In V_S configuration, due to the form of Mo-Mo metallic bonds (mentioned above), the unsaturated spin electrons are paired, extinguishing the magnetism. Thus, it is expected that the finding of elongation of d_{S-S} in the V_{Mo} defect (mentioned above) is advantageous for the magnetic induction. However, the energy difference between the spin-polarized state and spin-unpolarized state in the V_{Mo} configuration is only 5 meV,⁶⁵ indicating the very small stability of spin states. Considering the device applications, such spin polarized behaviors is impractical to use, since the thermal excitation to the nonmagnetic state can easily occur at room temperature. Thus, in order to conveniently compare with previous nonmagnetic results,³⁵ we also didn't highlight the unstable magnetic behavior of the V_{Mo} configuration. Fig. 1(c) gives band structures of MoS₂ sheet with V_S and V_{Mo} defects. Though the charge states of the native vacancies in the MoS₂ sheet can be 0, 2, +4, only the neutral native vacancies are considered in this work. Thus, the V_S defect as a donor can introduce four electrons to the system,

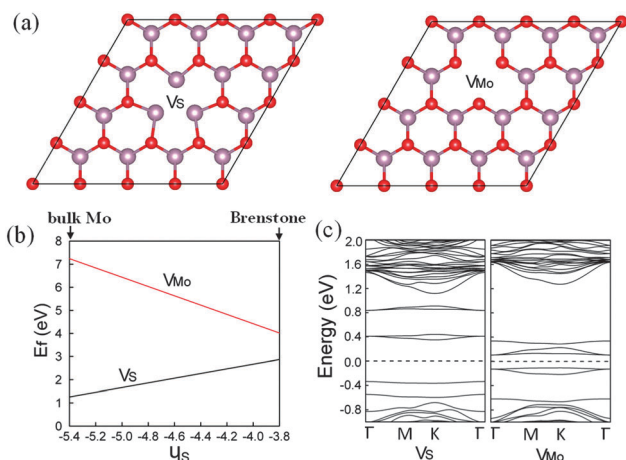


Fig. 1 (a) Optimized geometries for V_S and V_{Mo} structures. Small (red) and large (purple) balls represent S and Mo atoms, respectively. (b) Formation energies of V_S and V_{Mo} structures as a function of S chemical potential. (c) Energy band structures of V_S and V_{Mo} structures.

and V_{Mo} defect as an acceptor can leave four holes in the system. Consequently, in vacancy-induced MoS_2 sheet, several defect levels appear in the gap, which does not destroy the semiconducting behavior but decreases the band gap. Calculated band gaps of MoS_2 sheet become about 0.7 and 0.2 eV for V_{S} and V_{Mo} defects, respectively. In fact, vacancy-induced defect levels have been proposed in FeS_2 compound by qualitative ligand field theory⁶⁶ and DFT calculation.⁶⁷

3.3 MoS_2 nanoholes

Developing approaches to effectively induce and control the magnetic states is critical to the use of magnetic nanostructures in quantum information devices but is still challenging. The zigzag edges of different shaped nanoholes in graphene and BN sheet have been investigated, and as such were predicted to carry intriguing magnetic moments.^{45,68} Thus, the intensive studies of graphene and BN nanoholes inspired us to answer the question if the novel magnetic properties can be hold in MoS_2 -based nanoholes. We explore this by considering four representative defect structures (1) removing 12 S and 10 Mo atoms ($V_{12\text{S}+10\text{Mo}}$), (2) removing 20 S and 6 Mo atoms ($V_{20\text{S}+6\text{Mo}}$), (3) removing 16 S and 8 Mo atoms ($V_{16\text{S}+8\text{Mo}}$), and (4) removing 24 S and 12 Mo atoms ($V_{24\text{S}+12\text{Mo}}$). Both $V_{12\text{S}+10\text{Mo}}$ and $V_{20\text{S}+6\text{Mo}}$ structures yield triangle shaped nanoholes, while $V_{16\text{S}+8\text{Mo}}$ and $V_{24\text{S}+12\text{Mo}}$ structures present the rectangle and hexagon shaped nanoholes, respectively. Optimized geometries of these structures are given in Fig. 2. The distinct characteristic of these structures is the reconstruction of corner atoms. For example, the obtained S-S distances at the corner of $V_{12\text{S}+10\text{Mo}}$ and $V_{16\text{S}+8\text{Mo}}$ structures become about 2.9 Å, and the Mo-Mo distances at the corner of $V_{20\text{S}+6\text{Mo}}$ and $V_{16\text{S}+8\text{Mo}}$ structures become about 2.7 Å. Obviously, the neighboring S (or Mo) atoms at the corners are bound each other in these structures, which is important for the structural stability and magnetic magnitude.

In order to determine the relative stability of these structures, we first calculated the formation energies expressed as:

$$E_{\text{f}} = \left(E_{\text{V}} + \sum n_i \mu_i - E_{\text{MoS}_2} \right) / N_{\text{L}} \quad (2)$$

where E_{V} and E_{MoS_2} are total energies of the MoS_2 supercell with and without vacancy defects, μ_i ($i = \text{S}, \text{Mo}$) and n_i are the

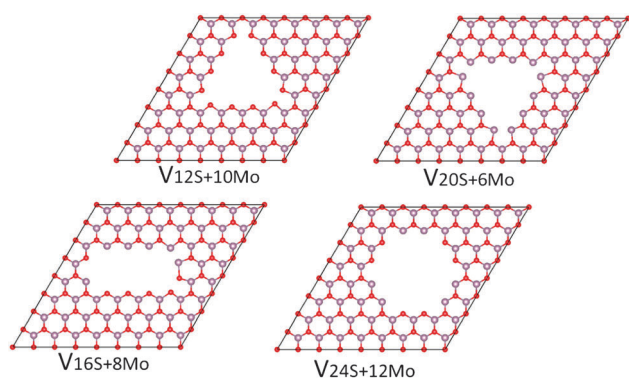


Fig. 2 Optimized geometries of different shaped nanoholes represented by $V_{12\text{S}+10\text{Mo}}$, $V_{20\text{S}+6\text{Mo}}$, $V_{16\text{S}+8\text{Mo}}$, and $V_{24\text{S}+12\text{Mo}}$, related with the edged length of 12.

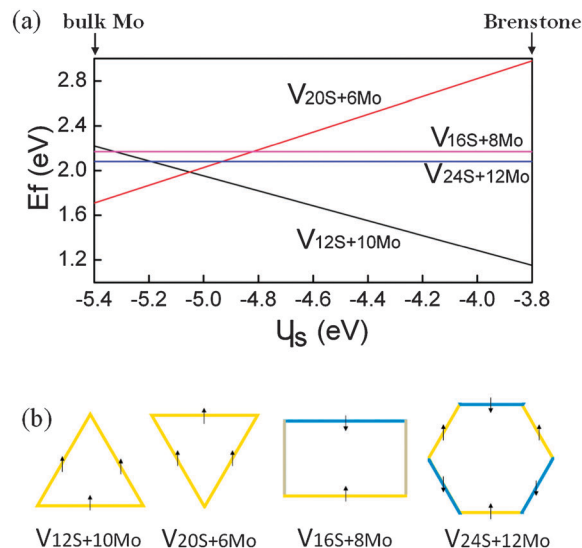


Fig. 3 (a) Formation energies of different shaped nanoholes as a function of S chemical potential. (b) The schematic illustration of cumulative spin around the edges of different shaped nanoholes.

chemical potential and number of removed i atoms, and N_{L} presents the zigzag edged length of nanohole. In order to allow direct comparison between the different shaped defects, we also assumed an equilibrium growth/annealing condition with a constraint, $2\mu_{\text{S}} + \mu_{\text{Mo}} = \mu_{\text{MoS}_2}$, where μ_{MoS_2} is the energy per MoS_2 pairs (−21.8 eV). At the onset, we may exclude the existence of rectangle and hexagon nanohole defects, since E_{f} of both structures are higher in all S environments, as shown in Fig. 3(a). The relative instability of these structures can be rationalized by the less corner bonds that only two and zero corner bonds are formed in rectangle and hexagon nanoholes, respectively. The plentiful unpaired dangling bonds enhance energies of both structures. On the contrary, triangle shaped nanoholes may have appreciable concentration in MoS_2 samples due to the relatively much corner bonds. For example, in S-rich conditions, calculated E_{f} of $V_{12\text{S}+10\text{Mo}}$ structure is only 1.2 eV, about 1.0 and 0.9 eV lower than rectangle and hexagon hole structures, respectively. Under S-poor conditions, the lowest E_{f} is about 1.7 eV found in $V_{20\text{S}+6\text{Mo}}$ structure, which is 0.5 and 0.4 eV lower than rectangle and hexagon holes structures, respectively. In fact, these situations are similar to that found in the BN sheet where the equilibrium nanoholes are nearly triangle shaped structures.⁵⁵

As reported in MoS_2 ribbons,⁴⁰ these unsaturated edged atoms in MoS_2 nanoholes should be responsible for the magnetic behavior. In order to illustrate this fact, we first calculated the energy difference between the spin-polarized and spin-unpolarized states, (about 330, 65, 207, and 410 meV for $V_{12\text{S}+10\text{Mo}}$, $V_{20\text{S}+6\text{Mo}}$, $V_{16\text{S}+8\text{Mo}}$ and $V_{24\text{S}+12\text{Mo}}$ structures, respectively), presenting the relative high stability of spin states. Fig. 3(b) gives the schematic illustration of cumulative spin around the edges of different shaped nanoholes. Obviously, all these structures have the intrinsic spin. However, only the triangle shaped nanoholes present the FM coupling characteristic

due to the chemically homogeneous edges, *i.e.*, only S- or Mo-terminated edges, giving the large magnetic moment. The moments (M) of S-terminated and Mo-terminated triangles can approximately satisfy $M = (N_L - 6)M_S$ and $M = (N_L - 6)M_{Mo}$, respectively. Here M_S (or M_{Mo}) denotes the spin moment of two S atoms (or single Mo atom) at the edge, and N_L presents the zigzag edged length of nanohole. In contrast, the net magnetisms in rectangle and hexagon nanoholes are small due to the nonequivalent edge structures in which an approximate AFM coupling characteristic was detected, and the moments of rectangle and hexagon nanoholes approximately satisfy $M = (N_L - 4)(M_{Mo} - M_S)/2$ and $M = N_L(M_{Mo} - M_S)/2$, respectively. In particular, armchair edges in rectangle structures don't contribute to the magnetism. Thus, based on above analysis, the triangle shaped nanohole holds the most potential for the actual magnetic applications in MoS_2 -based nanomaterials, which is similar to that found in graphene nanoholes.⁴⁴ In order to explore the valued magnetic behavior, *i.e.*, FM coupling, we mainly consider the triangle shaped nanoholes bellow. Fig. 4(a) and (b) give the spin states of un-optimized and optimized triangle shaped nanoholes, respectively. The contrast of spin states of these structures highlights the significant corner bond in which the electrons are paired and the magnetism was vanished. In fact, the corner bonds effect is consistent with previous findings in BN sheets.⁴⁵ For optimized structures, the spin states of $V_{12S+10Mo}$ and $V_{20S+6Mo}$ are mainly concentrated on the edged S and Mo atoms, respectively. Calculated spin moments of $V_{12S+10Mo}$ and $V_{20S+6Mo}$ structures are about 2.4 and 3.6 μ_B , respectively. (It should be noted that the spin polarization is not restricted only to the edge atoms at the extreme, and the next nearest neighbor atoms are also influenced to have a small degree of spin polarization). To get more details about the magnetic characteristic, we also computed spin-resolved partial density of states (PDOS) of optimized $V_{12S+10Mo}$ and $V_{20S+6Mo}$ structures, shown in Fig. 5. As expected, in $V_{12S+10Mo}$ structure, Mo atoms have symmetrical spin-up and spin-down states while the spin states in S atoms are asymmetrical. In contrast, the $V_{20S+6Mo}$ structure presents the opposite situation. Further examination of spin states shows that the asymmetrical features in $V_{12S+10Mo}$ and $V_{20S+6Mo}$ structures can be

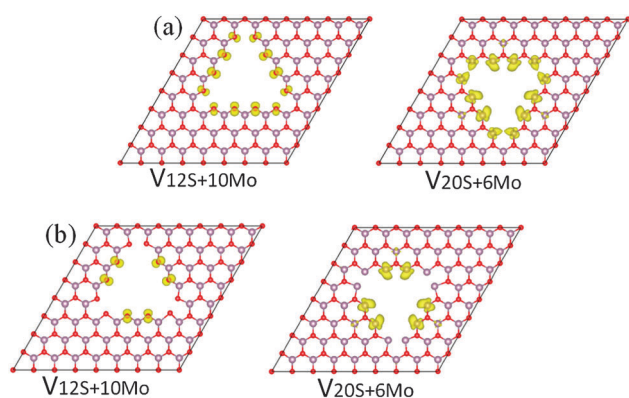


Fig. 4 Spatial spin density distributions ($\rho_{\text{spin-up}} - \rho_{\text{spin-down}}$) of (a) un-optimized and (b) optimized $V_{12S+10Mo}$ and $V_{20S+6Mo}$ nanohole structures.

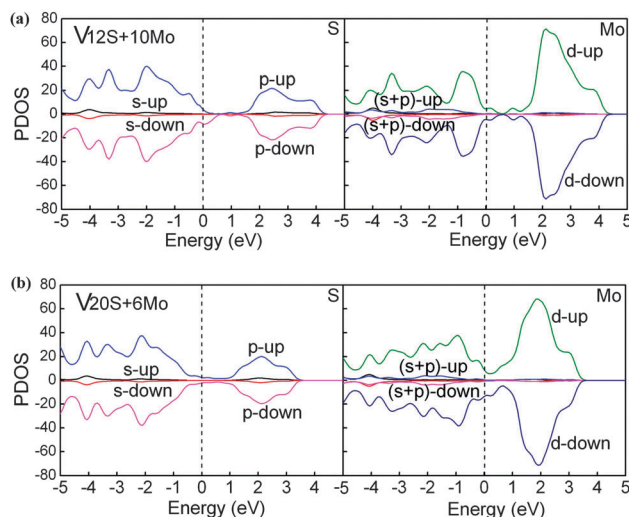


Fig. 5 Spin-polarized PDOS of optimized (a) $V_{12S+10Mo}$ and (b) $V_{20S+6Mo}$ nanohole structures.

ascribed to the partially filled S-2p orbitals and Mo-4d orbitals, respectively. Although the large triangular vacancy defects are not explored here due to the fact that a very large supercell has to be used to avoid the defect interaction between the periodic images and this exceeds the limitation of our computational resources, it is expected that the large vacancy defects should display substantial magnetism and high stability of spin states.

3.4 MoS_2 nanodots

Nanodots can be viewed as the structural complements to the vacancy defects explored above. Graphene and BN nanodots have been found to display intriguing electronic and magnetic properties.^{69,70} To conclude this discussion, we examined the stability and magnetic properties of four representative nanodots (1) consisting of 56 S and 21 Mo atoms ($D_{56S+21Mo}$), (2) consisting of 42 S and 28 Mo atoms ($D_{42S+28Mo}$), (3) consisting of 50 S and 25 Mo atoms ($D_{50S+25Mo}$), and consisting of 54 S and 27 Mo atoms ($D_{54S+27Mo}$). Fig. 6 gives optimized geometries of these structures. It can be seen that the geometries of these nanodots are nearly unchanged except a slight reconstruction at the corner in $D_{42S+28Mo}$ structure. Fig. 7(a) gives corresponding formation energies of these structures. Here the formation energies are calculated as follows:

$$E_f = (E_{MoS_2} + \sum n_i \mu_i) / N_L \quad (3)$$

where E_{MoS_2} is the energy of the MoS_2 nanodot, μ_i ($i = S, Mo$) and n_i are the chemical potential and number of i atoms, and N_L presents the edged length of the nanodot. Here we also assumed an equilibrium growth/annealing condition with a constraint $2\mu_S + \mu_{Mo} = \mu_{MoS_2}$. In Fig. 7(a), it is evident that E_f of $D_{56S+21Mo}$ structure is smaller than other structures in all S conditions, agreeing with the recent observation of S-terminated triangle nanodots.⁷¹ However, it doesn't mean that the shape of the MoS_2 nanodot must be restricted only to S-terminated triangle experimentally, since the E_f of $D_{42S+28Mo}$ and $D_{54S+27Mo}$

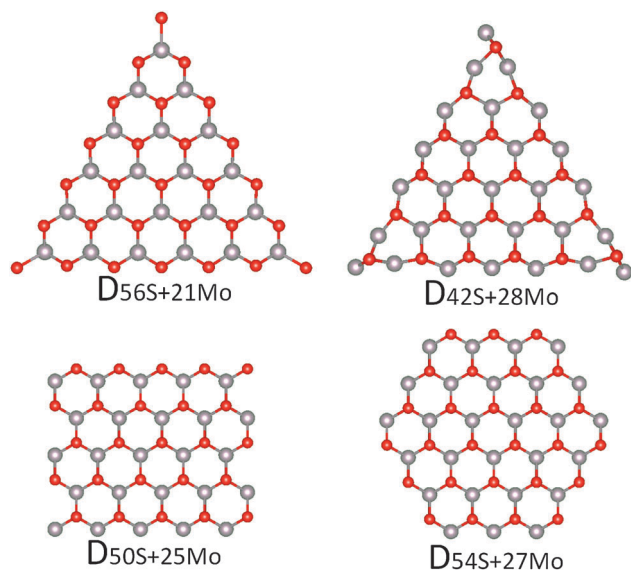


Fig. 6 Optimized geometries of different shaped nanodots represented $D_{56S+21Mo}$, $D_{42S+28Mo}$, $D_{50S+25Mo}$ and $D_{54S+27Mo}$, related with the edged length of 18.

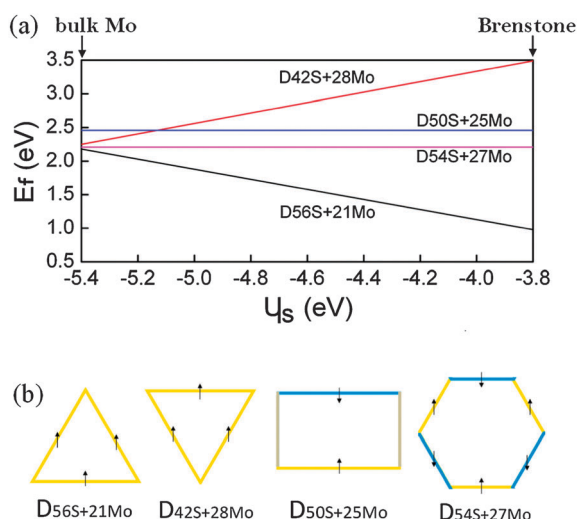


Fig. 7 (a) Formation energies of different shaped nanodots as a function of S chemical potential. (b) The schematic illustration of cumulative spin around the edges of different shaped nanodots.

structures are only 0.1 and 0.05 eV higher than that of the $D_{56S+21Mo}$ in S-poor condition.

When analyzing the magnetic behaviors of nanodots, the picture is similar to that found in nanoholes due to the similar edged characteristics. Calculated energy differences between the spin-polarized and spin-unpolarized states are about 910, 95, 260 and 530 meV for $D_{56S+21Mo}$, $D_{42S+28Mo}$, $D_{50S+25Mo}$ and $D_{54S+27Mo}$ structures, respectively, suggesting the relative high stability of spin states. Due to the difference of S and Mo sublattices, the magnetic behaviors of nanodots correlate to their shapes, as illustrated in Fig. 7(b). Examination from spin states shows that only triangle nanodots can be FM coupled, while rectangle and hexagon nanodot structures

display nearly AFM coupled characteristics. These findings are agreement with that in MoS_2 nanoholes. Thus, the structure of triangle nanodots is expected for the achievement of a large moment, and the net moments of S-terminated and Mo-terminated triangle nanodots can approximately satisfy $M = N_L M_S$ and $M = (N_L - 9) M_{Mo}$, respectively. Here M_S (or M_{Mo}) denotes the spin moment of two S atoms (or single Mo atom) at the edge, and N_L presents the zigzag edged length of nanodot. The total spin scales linearly with the size of nanodots, demonstrating a possibility of achievement of remarkable magnetism in both structures. When N_L reaches 18, spin moments become about 7.2 and 5.4 μ_B for $D_{56S+21Mo}$ and $D_{42S+28Mo}$ structures, respectively. Although these nanodots contain the similar magnetic behaviors as reported in nanoholes, understanding the properties of nanodots is important because the basic functional components of future electronics or spintronics devices will need to be at the nanometer scale to uphold the trend of increased performance with miniaturization.

In view of the potential spin applications of these nanodots, we proposed a simple model, as shown in Fig. 8(a), in which a nanodot is sandwiched between two conducting metal lines. This model was prompted by a recent report where a graphene nanodot linked by Au nanowires was used to investigate transport characteristics.⁷² It can be concluded that the spin states in the $D_{56S+21Mo}$ structure mainly locate at edged S atoms, presenting a collective characteristic with a same spin alignment. As a comparison, the collective characteristic in the $D_{42S+28Mo}$ structure disappeared due to the formation of corner Mo–Mo bonds. It is well known that for a magnetic system one of the crucial issues for its applications in spintronic devices is whether the local spin moment can lead to a collective characteristic, which is an essential requirement for any spintronic applications. Unfortunately, this critical issue, as well as its implications, was often overlooked in previous studies. Thus, the finding of a substantial collective characteristic in the $D_{56S+21Mo}$ structure offers a potential to achieve the excellent transmission channel for the single-spin electrons. However, in order to achieve this goal, the particular electronic properties near the Fermi level must be considered. Fig. 8(b) gives the PDOS of Mo and S atoms of $D_{56S+21Mo}$ structure. As expected, the states of S atoms display a complete spin-polarization around the Fermi level with the intrinsic spin transport anisotropy, *i.e.*, half-metallicity, mainly contributed by S-2p orbitals, which enables zigzag edged S atoms to possess an intrinsic spin filtering characteristic. In contrast, Mo atoms have symmetrical spin-up and spin-down states, and thus didn't effect the magnetic property. For other nanodot structures, such as $D_{50S+25Mo}$ and $D_{54S+27Mo}$, our examination of PDOS shows the metallic characteristic for both spin-up and spin-down states, indicating that the electrons will transport across these nanodots without the spin separateness. Thus, based on these findings, the transport properties can be engineered by controlling the shape of nanodots, and the S-terminated triangle nanodot offers a large potential to achieve single-spin devices.

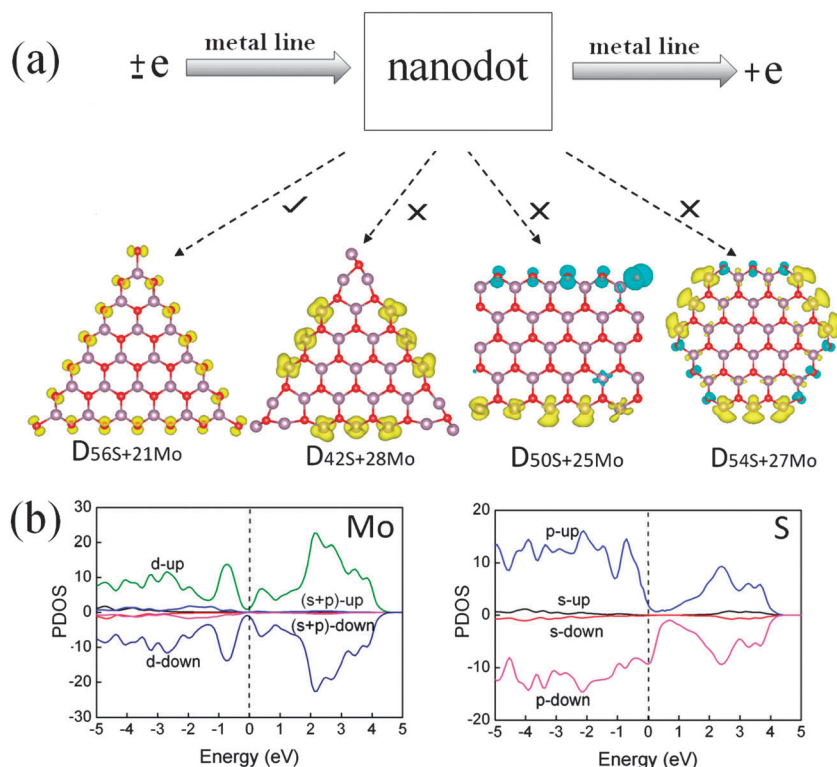


Fig. 8 (a) Schematic illustration of different shaped nanodots sandwiched between two conducting metal lines forming a possible spin switch device. The spatial spin density distributions of sandwiched nanodots are plotted. (b) Spin-polarized PDOS of D56S+21Mo nanodot structure.

3.5 MoS₂ antidots

As recently reported in graphene, state-of-the-art e-beam lithography has been used to create regular antidot lattices.⁵⁸ We expect the same technique would be used in MoS₂ sheet. In fact, the geometry of the MoS₂ antidot superlattice can be viewed as the integration of nanoholes and nanodots. Here three antidots, *i.e.*, only S-terminated antidots (A_{S-S-S-S}), only Mo-terminated antidots (A_{Mo-Mo-Mo-Mo}), and S-terminal and Mo-terminal coexisted antidots (A_{S-Mo-S-Mo} and A_{S-S-Mo-Mo}), were examined, as shown in Fig. 9. These types of antidots could be very interesting for building 2D magnetic nano-materials, since each type includes a large number of triangular nanoholes with FM coupling (mentioned above), giving a potential to possess a large spin moment. However, in order to achieve this goal, the coupled interaction between nearby nanoholes must be considered, since the magnitude of net spin depends on not only the local nanohole spin property but also the long-range coupled interaction between nanoholes. Thus, in order to determine the coupled interaction, the energy difference between AFM and FM states, $\Delta E = E_{\text{AFM}} - E_{\text{FM}}$, was first calculated. Obtained ΔE are about 288 and 120 meV for A_{S-S-S-S} and A_{Mo-Mo-Mo-Mo} structures, respectively, presenting the favored FM coupling. However, in A_{S-Mo-S-Mo} and A_{S-S-Mo-Mo} structures, the AFM coupling becomes favored, associated with the energy difference of 190 meV for both structures. These results strongly suggest the existence of coupled connection between nearby nanoholes in the MoS₂ antidot superlattice.

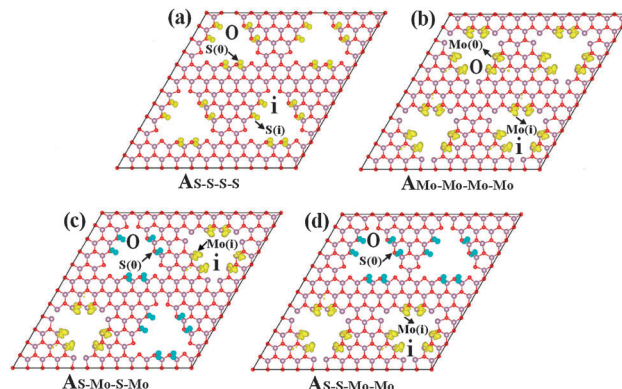


Fig. 9 Spatial spin density distributions of (a) only S-terminated antidot (A_{S-S-S-S}), (b) only Mo-terminated antidot (A_{Mo-Mo-Mo-Mo}), and S-terminal and Mo-terminal coexisted antidots (c) (A_{S-Mo-S-Mo}) and (d) (A_{S-S-Mo-Mo}). In these antidot structures, S(0) and S(i) represent the terminated S atoms surrounding the nanoholes 0 and i, respectively, and Mo(0) and Mo(i) represent the terminated Mo atoms surrounding the nanoholes 0 and i, respectively.

A corresponding coupling mechanism, *i.e.*, through-bond coupling interaction has been successfully proposed by Jin *et al.*⁷³ For through-bond coupling interaction, an atom with up-spin (or down-spin) density can induce a down-spin (or up-spin) density on the adjacent atom directly bonded to it. Thus, all S atoms in a MoS₂ antidot relate with the same spin order, and all Mo atoms in MoS₂ antidot relate with the other spin order. According to currently calculated results, this mechanism also

holds well. For example, in the A_{S-S-S} structure, provided that $S(0)$ and $S(i)$ represent the terminated S atoms surrounding the nanoholes 0 and i , respectively, the through-bond spin polarization will take place along the $S(0) \rightarrow Mo \rightarrow n(S \rightarrow Mo) \rightarrow S(i)$ ($n = 0, 1, 2, 3, \dots$) path. Consequently, nanoholes 0 and i in the A_{S-S-S} structure present FM coupled characteristics due to the same spin order of $S(0)$ and $S(i)$ atoms, as shown in Fig. 9(a). A similar situation was detected in the $A_{Mo-Mo-Mo-Mo}$ structure, in which provided that $Mo(0)$ and $Mo(i)$ represent the terminated Mo atoms surrounding the nanoholes 0 and i , the through-bond spin polarization will take place along the $Mo(0) \rightarrow S \rightarrow n(Mo \rightarrow S) \rightarrow Mo(i)$ ($n = 0, 1, 2, 3, \dots$) path. Thus, nanoholes 0 and i in the $A_{Mo-Mo-Mo-Mo}$ structure also present the FM coupled characteristic due to the same spin order of $Mo(0)$ and $Mo(i)$ atoms, as shown in Fig. 9(b). As a matter of fact, the interaction of through-bond coupling has also been previously reported to explain the room-temperature FM characteristic in half-fluorinated graphene, BN and GaN sheets.⁷⁴ Thus, due to the long-range FM coupling, both A_{S-S-S} and $A_{Mo-Mo-Mo-Mo}$ structures display a potential to possess the large spin moment. However, the situations in $A_{S-Mo-S-Mo}$ and $A_{S-S-Mo-Mo}$ structures are very different. Provided that $S(0)$ and $Mo(i)$ represent the terminated S and Mo atoms surrounding the nanoholes 0 and i , respectively. The through-bond spin polarization will take place along $S(0) \rightarrow n(Mo \rightarrow S) \rightarrow Mo(i)$ ($n = 0, 1, 2, 3, \dots$) path. Nanoholes in both $A_{S-Mo-S-Mo}$ and $A_{S-S-Mo-Mo}$ structures give an AFM coupling due to the opposite spin order of $S(0)$ and $Mo(i)$ atoms, which leads to the small magnetic moment, as shown in Fig. 9(c) and (d). This is disadvantageous for the achievement of our goal of the large magnetism. Fortunately, based on the analysis of E_f of different shaped nanoholes (mentioned in Section (iii)), control of the S condition (only in rich or poor condition) will allow one to generate single-typed triangle nanoholes in the MoS_2 sheet, *i.e.*, only S-terminated triangle nanoholes such as A_{S-S-S} structure or only Mo-terminated triangle nanoholes such as $A_{Mo-Mo-Mo-Mo}$ structure, giving great benefit for generating large magnetism. To probe whether these antidot superlattices can support spin coupling above the room temperature, we estimate the Curie temperature (T_C) of these structures according to the Heisenberg model. The magnetic energy difference can be described using the mean-field value of T_C with $k_B T_C = (2/3)|\Delta E|$.⁷³ Calculated T_C for A_{S-S-S} , $A_{Mo-Mo-Mo-Mo}$, $A_{S-Mo-S-Mo}$ and $A_{S-S-Mo-Mo}$ structures are about 557, 232, 398 and 400 K, respectively. The values of A_{S-S-S} , $A_{S-Mo-S-Mo}$ and $A_{S-S-Mo-Mo}$ structures are higher than the room temperature, suggesting the relative stable spin states of FM coupling in A_{S-S-S} structure and AFM coupling in $A_{S-Mo-S-Mo}$ and $A_{S-S-Mo-Mo}$ structures. However, it should be noted that the stability of spin states is easy to reduce, since if the distance between the nearby nanoholes was large enough the through-bond coupling interaction becomes weak and the ΔE will decrease to a very small value. Thus, the magnetic properties, such as the net spin, coupled order and the stability of spin states in antidot superlattices can be engineered by controlling the type and distance of internal nanoholes, providing a

theoretical insight into the experimental exploration of MoS_2 -based magnetic devices at the nanometer scale.

4. Conclusion

Developing approach to effectively induce and control the magnetic states is critical to the use of magnetic nanostructures in quantum information devices but is still challenging. Using density functional theory, we systematically explore structural stability, electronic and magnetic properties of MoS_2 -based nanostructures, such as atomic defects, nanoholes, nanodots and antidots. The S-vacancy defect is most energetically favorable in all S conditions, which may clarify the preferred origin for the further formation of nanoholes. Among different shaped nanoholes, triangle ones are most energetically favorable, and exhibit an unexpected large spin moment that is scaled linearly with edged length. In nanodots, the general situation is the same as that found in nanoholes due to similar edge properties. However, it is interesting to find that S-terminated triangle nanodots shows strong spin anisotropy around the Fermi level with a substantial collective characteristic of spin states at edges, enabling it to a desired spin-filtering structure. In antidots, the net spin, coupled order and stability of spin states can be engineered by controlling type and distance of internal nanoholes. In particular, the only S-terminated antidots can exhibit a large net spin above room temperature. Given the recent achievement of graphene- and BN-based nanohole, nanodot and antidot structures, we believe that our calculated results are suitable for experimental verification and implementation giving a new path to explore MoS_2 -based magnetic nanostructures.

Acknowledgements

This work was supported by the Fundamental Research Funds for the Central Universities. Ping Yang acknowledges partial support from the Environmental Molecular Sciences Laboratory (EMSL) through its intramural program. A portion of this research was performed using the Environmental Molecular Sciences Laboratory, a national scientific user facility sponsored by the U.S. Department of Energy's Office of Biological and Environmental Research, located at Pacific Northwest National Laboratory (PNNL). PNNL is operated by Battelle for the U.S. Department of Energy.

References

- 1 V. V. Ivanovskaya, A. Zobelli, A. Gloter, N. Brun, V. Serin and C. Colliex, *Phys. Rev. B: Condens. Matter Mater. Phys.*, 2008, **78**, 134104.
- 2 S. Lebègue and O. Eriksson, *Phys. Rev. B: Condens. Matter Mater. Phys.*, 2009, **79**, 115409.
- 3 A. Kuc, N. Zibouche and T. Heine, *Phys. Rev. B: Condens. Matter Mater. Phys.*, 2011, **83**, 245213.
- 4 A. Ramasubramaniam, D. Naveh and E. Towe, *Phys. Rev. B: Condens. Matter Mater. Phys.*, 2011, **84**, 205325.

- 5 M. Topsakal and S. Ciraci, *Phys. Rev. B: Condens. Matter Mater. Phys.*, 2012, **85**, 045121.
- 6 Y. D. Ma, Y. Dai, W. Wei, C. W. Niu, L. Yu and B. B. Huang, *J. Phys. Chem. C*, 2011, **115**, 20237.
- 7 Y. D. Ma, Y. Dai, M. Guo, C. W. Niu and B. B. Huang, *Nanoscale*, 2011, **3**, 3883.
- 8 R. H. Friend and A. D. Yoffe, *Adv. Phys.*, 1987, **36**, 1.
- 9 Y. Y. Peng, Z. Y. Meng, C. Zhong, J. Lu, W. C. Yu, Y. B. Jia and Y. T. Qian, *Chem. Lett.*, 2001, 772.
- 10 Z. Z. Wu, D. Z. Wang, X. Q. Zan and A. K. Sun, *Mater. Lett.*, 2010, **64**, 856.
- 11 B. Radisavljevic, A. Radenovic, J. Brivio, V. Giacometti and A. Kis, *Nat. Nanotechnol.*, 2011, **6**, 147.
- 12 Z. Y. Yin, H. Li, L. Jiang, Y. M. Shi, Y. H. Sun, G. Lu, Q. Zhang, X. D. Chen and H. Zhang, *ACS Nano*, 2012, **6**, 74.
- 13 G. Eda, H. Yamaguchi, D. Voiry, T. Fujita, M. W. Chen and M. Chhowalla, *Nano Lett.*, 2011, **11**, 5111.
- 14 M. Thomalla and H. Tributsch, *J. Phys. Chem. B*, 2006, **110**, 12167.
- 15 K. H. Hu, X. G. Hu, Y. F. Xu and X. Z. Pan, *React. Kinet., Mech. Catal.*, 2010, **100**, 153.
- 16 A. M. Seayad and D. M. Antonelli, *Adv. Mater.*, 2004, **16**, 765.
- 17 M. Mosleh, N. D. Atnafu, J. H. Belk and O. M. Nobles, *Wear*, 2009, **267**, 1220.
- 18 K. Chang and W. X. Chen, *ACS Nano*, 2011, **5**, 4720.
- 19 K. Chang, W. X. Chen, L. Ma, H. Li, H. Li, F. H. Huang, Z. D. Xu, Q. B. Zhang and J. Y. Lee, *J. Mater. Chem.*, 2011, **21**, 6251.
- 20 A. Molina-Sánchez and L. Wirtz, *Phys. Rev. B: Condens. Matter Mater. Phys.*, 2011, **84**, 155413.
- 21 K. Kaasbjerg, K. S. Thygesen and K. W. Jacobsen, *Phys. Rev. B: Condens. Matter Mater. Phys.*, 2012, **85**, 115317.
- 22 M. V. Bollinger, J. V. Lauritsen, K. W. Jacobsen, J. K. Nørskov and S. Helveg, *Phys. Rev. Lett.*, 2001, **87**, 196803.
- 23 C. Ataca, H. Sahin, E. Akturk and S. Ciraci, *J. Phys. Chem. C*, 2011, **115**, 3934.
- 24 A. Vojvodic, B. Hinnemann and J. K. Nørskov, *Phys. Rev. B: Condens. Matter Mater. Phys.*, 2009, **80**, 125416.
- 25 H. Schweiger, P. Raybaud, G. Kresse and H. Toulhoat, *J. Catal.*, 2002, **207**, 76.
- 26 M. V. Bollinger, K. W. Jacobsen and J. K. Nørskov, *Phys. Rev. B: Condens. Matter*, 2003, **67**, 085410.
- 27 H. Pan and Y. W. Zhang, *J. Mater. Chem.*, 2012, **22**, 7280.
- 28 Z. Y. Wang, H. Li, Z. Liu, Z. J. Shi, J. Lu, K. Suenaga, S. K. Joong, T. Okazaki, Z. N. Gu, J. Zhou, Z. X. Gao, G. P. Li, S. Sanvito, E. G. Wang and S. Iijima, *J. Am. Chem. Soc.*, 2010, **132**, 13840.
- 29 Y. Y. Liu, S. Bhowmick and B. I. Yakobson, *Nano Lett.*, 2011, **11**, 3113.
- 30 W. S. Yun, S. W. Han, S. C. Hong, I. G. Kim and J. D. Lee, *Phys. Rev. B: Condens. Matter Mater. Phys.*, 2012, **85**, 033305.
- 31 J. K. Ellis, M. J. Lucero and G. E. Scuseria, *Appl. Phys. Lett.*, 2011, **99**, 261908.
- 32 E. Scalise, M. Houssa, G. Pourtois, V. Afanas'ev and A. Stesmans, *Nano Res.*, 2012, **5**, 43.
- 33 D. Le, D. Z. Sun, W. H. Lu, L. Bartels and T. S. Rahman, *Phys. Rev. B: Condens. Matter Mater. Phys.*, 2012, **85**, 075429.
- 34 I. Popov, G. Seifert and D. Tománek, *Phys. Rev. Lett.*, 2012, **108**, 156802.
- 35 C. Ataca and S. Ciraci, *J. Phys. Chem. C*, 2011, **115**, 13303.
- 36 Y. D. Ma, Y. Dai, M. Guo, C. W. Niu, Y. T. Zhu and B. B. Huang, *ACS Nano*, 2012, **6**, 1695.
- 37 K. Dolui, C. D. Pemmaraju and S. Sanvito, *ACS Nano*, 2012, **6**, 4823.
- 38 O. V. Yazyev, *Rep. Prog. Phys.*, 2010, **73**, 056501.
- 39 J. H. Yang, D. Y. Kim, J. S. Hong and X. H. Qian, *Surf. Sci.*, 2010, **604**, 1603.
- 40 Y. F. Li, Z. Zhou, S. B. Zhang and Z. F. Chen, *J. Am. Chem. Soc.*, 2008, **130**, 16739.
- 41 F. W. Zheng, G. Zhou, Z. R. Liu, J. Wu, W. H. Duan, B. L. Gu and S. B. Zhang, *Phys. Rev. B: Condens. Matter Mater. Phys.*, 2008, **78**, 205415.
- 42 E. Kan, H. J. Xiang, F. Wu, C. Lee, J. L. Yang and M. Whangbo, *Appl. Phys. Lett.*, 2010, **96**, 102503.
- 43 B. Huang, H. Lee, B. L. Gu, F. Liu and W. H. Duan, *Nano Res.*, 2012, **5**, 62.
- 44 W. L. Wang, S. Meng and E. Kaxiras, *Nano Lett.*, 2008, **8**, 241.
- 45 A. J. Du, Y. Chen, Z. H. Zhu, R. Amal, G. Q. Lu and S. C. Smith, *J. Am. Chem. Soc.*, 2009, **131**, 17354.
- 46 D. C. Yu, E. M. Lupton, M. Liu, W. Liu and F. Liu, *Nano Res.*, 2008, **1**, 56.
- 47 F. P. Ouyang, S. L. Peng, Z. F. Liu and Z. R. Liu, *ACS Nano*, 2011, **5**, 4023.
- 48 J. Y. Huang, L. Qi and J. Li, *Nano Res.*, 2010, **3**, 43.
- 49 S. Matsui and Y. Ochiai, *Nanotechnology*, 1996, **7**, 247.
- 50 J. M. Gibson, *Phys. Today*, 1997, **50**, 56.
- 51 M. D. Levenson, *Solid State Technol.*, 1995, **38**, 81.
- 52 M. H. Gass, U. Bangert, A. L. Bleloch, P. Wang, R. R. Nair and A. K. Geim, *Nat. Nanotechnol.*, 2008, **3**, 676.
- 53 K. Suenaga, H. Kobayashi and M. Koshino, *Phys. Rev. Lett.*, 2012, **108**, 075501.
- 54 N. Alem, O. V. Yazyev, C. Kisielowski, P. Denes, U. Dahmen, P. Hartel, M. Haider, M. Bischoff, B. Jiang, S. G. Louie and A. Zettl, *Phys. Rev. Lett.*, 2011, **106**, 126102.
- 55 C. H. Jin, F. Lin, K. Suenaga and S. Iijima, *Phys. Rev. Lett.*, 2009, **102**, 195505.
- 56 B. Song, G. F. Schneider, Q. Xu, G. Pandraud, C. Dekker and H. Zandbergen, *Nano Lett.*, 2011, **11**, 2247.
- 57 A. L. Vazquez de Parga, F. Calleja, B. Borca, M. C. G. P. Jr, J. J. Hinarejos, F. Guinea and R. Miranda, *Phys. Rev. Lett.*, 2008, **100**, 056807.
- 58 M. Kim, N. S. Safron, E. Han, M. S. Arnold and P. Gopaland, *Nano Lett.*, 2010, **10**, 1125.
- 59 H. P. Komsa, J. Kotakoski, S. Kurasch, O. Lehtinen, U. Kaiser and A. V. Krashennnikov, *Phys. Rev. Lett.*, 2012, **109**, 035503.
- 60 J. V. Lauritsen, J. Kibsgaard, S. Helveg, H. Topsoe, B. S. Clausen, E. Lægsgaard and F. Besenbacher, *Nat. Nanotechnol.*, 2007, **2**, 53.
- 61 C. Ataca and S. Ciraci, *Phys. Rev. Lett.*, 2012, **85**, 195410.

- 62 C. Ataca, M. Topsakal, E. Akturk and S. Ciraci, *J. Phys. Chem. C*, 2011, **115**, 16354.
- 63 S. Azevedo, J. R. Kaschny, C. M. C. Castilho and F. B. Mota, *Nanotechnology*, 2007, **18**, 495707.
- 64 A. K. Singh, E. S. Penev and B. I. Yakobson, *ACS Nano*, 2010, **4**, 3510.
- 65 J. Zhang, J. M. Soon, K. P. Loh, J. H. Yin, J. Ding, M. B. Sullivan and P. Wu, *Nano Lett.*, 2007, **7**, 2370.
- 66 M. Birkholz, S. Fiechter, A. Hartmann and H. Tributsch, *Phys. Rev. B: Condens. Matter*, 1991, **43**, 11926.
- 67 J. Hu, Y. N. Zhang, M. Law and R. Wu, *Phys. Rev. B: Condens. Matter Mater. Phys.*, 2012, **85**, 085203.
- 68 F. P. Ouyang, Z. X. Yang, J. Xiao, D. Wu and H. Xu, *J. Phys. Chem. C*, 2010, **114**, 15578.
- 69 S. S. Yu, W. T. Zheng, C. Wang and Q. Jiang, *ACS Nano*, 2010, **4**, 7619.
- 70 Y. Xi, M. W. Zhao, X. P. Wang, S. J. Li, X. J. He, Z. H. Wang and H. X. Bu, *J. Phys. Chem. C*, 2011, **115**, 17743.
- 71 S. Helveg, J. V. Lauritsen, E. Lægsgaard, I. Stensgaard, J. K. Nørskov, B. S. Clausen, H. Topsøe and F. Besenbacher, *Phys. Rev. Lett.*, 2000, **84**, 951.
- 72 W. Sheng, Z. Y. Ning, Z. Q. Yang and H. Guo, *Nanotechnology*, 2010, **21**, 385201.
- 73 H. Jin, Y. Dai, B. B. Huang and M.-H. Whangbo, *Appl. Phys. Lett.*, 2009, **94**, 162505.
- 74 Y. D. Ma, Y. Dai, M. Guo, C. Niu, L. Yu and B. Huang, *Nanoscale*, 2011, **3**, 2301.